

Enhancing Electrochemical Properties of Walnut Shell Activated Carbon with Embedded MnO Clusters for Supercapacitor Applications

Daniel Arenas Esteban,*^[a, b] Elena García Chamocho,^[a] Javier Carretero González,^[c] Esteban Urones Garrote,^[d] Luis Carlos Otero Díaz,^[a] and David Ávila Brande*^[a]

Activated carbon (AC) materials from renewable sources are widely used in electrochemical applications due to their well-known high surface area. However, their application as electrode material in double-layer electrochemical devices may be limited due to their relatively low electrical conductivity and lightweight. To overcome these limitations, the incorporation of pseudocapacitance metal oxide nanoparticles is an optimum approach. These nanoparticles can provide a second energy storage mechanism to the composite, mitigating the loss of surface area associated with their incorporation. As a result, the composite material is endowed with increased conductivity and higher density, making it more suitable for practical implementation in real devices. In this study, we have incorporated a fine

dispersion of 1% of MnO clusters into a highly porous activated carbon synthesized from walnut shells (WAC). The high-resolution electron microscopy studies, combined with their related analytical techniques, allow us to determine the presence of the cluster within the matrix carbon precisely. The resulting MnO@WAC composite demonstrated significantly improved capacitive behavior compared with the WAC material, with increased volumetric capacitance and higher charge retention at higher current densities. The composite's electrochemical performance suggests its potential as a promising electrode material for supercapacitors, addressing drawbacks associated with traditional AC materials.

Introduction

The shift from fossil fuels to renewable energy sources is creating a pressing need for advanced energy storage systems that can adjust to the irregular and intermittent nature of renewable energy.^[1] As example, solar energy is only available during the day and wind energy is dependent on weather

conditions. Electric double-layer capacitors (EDLCs),^[2] also known as supercapacitors, have become increasingly important in managing such energy fluctuations. These devices are the most efficient energy storage devices that can adapt to unpredictable energy peaks due to their well-known power density and fast response.^[3]

Currently, most commercial Electric Double-Layer Capacitors (EDLCs) utilize Activated Carbon (AC) as the primary electrode material. This preference is due to the well-established manufacturing processes, ease of large-scale production, relatively low cost, and excellent cycle stability of AC.^[4] Over the past few years, it has been discovered by researchers that certain natural resources that possess substantial amounts of biomass, such as wood, bamboo, coconut shells, and olive pits, can be utilized to produce activated carbons (ACs).^[5] These materials exhibit significant surface areas exceeding $2,000 \text{ m}^2 \text{ g}^{-1}$ and can achieve specific capacitances surpassing 200 F g^{-1} in organic electrolytes.^[6] However, they may encounter challenges related to conductivity and density, which can affect performance, especially during packing for electrode material formation.^[7]

In classic supercapacitors, the energy storage mechanism stems from the formation of an electric double layer at the electrode/electrolyte interface.^[8] Generally, a larger surface area of the electrode leads to higher capacitance, although the configuration of the porous structure also plays a critical role.^[9] Additionally, transition metal oxides or conductive polymers can store energy through a different mechanism known as pseudo-capacitance.^[10] The phenomenon of pseudo-capacitance bears a resemblance to classical capacitance in that it is

[a] D. A. Esteban, E. G. Chamocho, L. C. Otero Díaz, D. Á. Brande
Inorganic Chemistry Department
Faculty of Chemical Sciences
Complutense University of Madrid
Avenida Complutense s/n, 28040 Madrid, Spain
E-mail: daniel.arenasesteban@uantwerpen.be
davilab@ucm.es

[b] D. A. Esteban
Electron Microscopy for Materials Science (EMAT)
and NANOLab Center of Excellence
University of Antwerp
Groenenborgerlaan 171, 2020 Antwerp, Belgium

[c] J. Carretero González
Institute of Polymer Science and Technology, ICTP, CSIC
Calle Juan de la Cierva 3, 28006 Madrid, Spain

[d] E. Urones Garrote
CNM-ELECM - National Center for Electron Microscopy,
Faculty of Chemical Sciences
Complutense University of Madrid
Avenida Complutense s/n, 28040 Madrid, Spain

 Supporting information for this article is available on the WWW under
<https://doi.org/10.1002/batt.202400101>

 © 2024 The Authors. *Batteries & Supercaps* published by Wiley-VCH GmbH.
This is an open access article under the terms of the Creative Commons Attribution License, which permits use, distribution and reproduction in any medium, provided the original work is properly cited.

also a surface-bound process. In this type of capacitance, rapid and reversible surface reactions are triggered by the redox reactions taking place between the electrode and the electrolyte. During the Faradaic process, electrons generated by the redox reaction are transferred across the interface of the electrode and the electrolyte. It is worth noting that this process occurs at the nanoscale, and its efficiency depends on the nature of the electrode material, as well as the electrolyte used.^[11]

While ruthenium oxide (RuO_2) stands out as an exemplary pseudocapacitive material,^[12] its shortage and high market price limit applications primarily to military and aerospace industries.^[13] Manganese is the 12th most abundant element on Earth's crust. It is cheap, environmentally friendly, and available in various oxidation states. Manganese, abundant and cost-effective, emerges as a promising alternative for electrochemical purposes. Manganese oxides (MnO_x) exhibit remarkable pseudocapacitive activity, with nanoparticles presenting larger surface areas, thereby enhancing pseudocapacitive performance and reducing current densities.^[14]

The incorporation of MnO_x nanoparticles into AC materials presents a compelling solution to address the limitations of AC in terms of electric conductivity and low density, thanks to the pseudocapacitive nature of the nanoparticles. By decorating carbons at the nanoscale with this "battery-like" material, a Faradaic charge transfer is enabled, resulting in an improved total specific capacitance for the composite materials. Consequently, numerous studies have explored $\text{MnO}_x@\text{carbon}$ composite systems for applications in supercapacitors.^[15] The use of MnO_2 has become one of the standard oxidation states used from manganese, with its storage mechanism having been extensively studied.^[16] Intriguingly, it has also been observed that MnO possesses higher performance, although the storage mechanism remains unclear.

In this study, our aim was to elevate the electrochemical characteristics of activated carbon (AC) derived from walnut shells (*Juglans Regia*) by incorporating a mere ~1% of MnO clusters, each approximately 2 nm in size, finely dispersed within the carbon matrix. This deliberate addition serves to minimize the additional cost of this innovative composite material. The AC derived from *Juglans Regia* (WAC) demonstrates a volumetric capacitance of 38 F cm^{-3} when measured at 1 A g^{-1} in an aqueous (KCl) electrolyte. This performance matches and even surpasses values reported in literature for AC derived from lignocellulosic precursors.^[17] However, the capacitance experiences a notable decrease as the current rate increases, attributed not only to the presence of surface oxygenated acidic groups^[18] but also to the low electronic conductivity of activated carbon, typically ranging from 10 to 100 S m^{-1} . The synthesized $\text{MnO}@\text{WAC}$ composite yields 48 F cm^{-3} , representing an increase of 26% of the total capacitance compared to the AC material, despite a 29% reduction in surface area due to cluster deposition. Additionally, the composite material notably outperforms the capacitance retention at higher current densities, retaining 63% of its total capacitance at two orders of magnitude higher currents, while the AC material loses all capacitance at similar rates. This

indicates that the composite material has great potential for real-world applications.

Results and Discussion

Structural Characterization

Walnut shells are a low-cost, renewable biomass with a high lignin content, making them an excellent precursor material. Table 1 presents the elemental analysis results conducted on walnut shells (*Juglans Regia*) and the activated carbon derived from them. The analysis confirms that both the walnut shell and the activated carbon derived from walnut shells (WAC) have a high carbon content.

The carbon content nearly doubled after carbonization and chemical activation (reaching 85.3%). However, the presence of surface oxygenated acidic groups, including quinones or hydroquinones, can be attributed to the essential oxygen and hydrogen concentrations detected. These concentrations are responsible for the surface's acidic nature. These oxygenated surface groups were identified using infrared spectroscopy (IR). The spectrum exhibits a broad band centered at $1,579 \text{ cm}^{-1}$, indicating the presence of quinonic groups ($\nu(\text{C=O})$). Bands within the range of $1,375$ - $1,427 \text{ cm}^{-1}$ correspond to the stretching vibrations of $\nu(\text{C-O})$, revealing the formation of xantenes and ethers (see Figure S.1).

The scanning electron microscopy (SEM) images presented in Figure 1 enable a direct comparison of the morphology between the precursor and the activated carbon (AC). While the precursor exhibits a smooth and flat surface (Figure 1a), the AC displays surface roughness, clearly indicating the effects of the

Table 1. Elemental analysis from the precursor and the WAC (%).

	C	N	H	O
Juglans regia	48.04	6.01	0.30	45.51
WAC	85.30	0.32	0.91	13.43

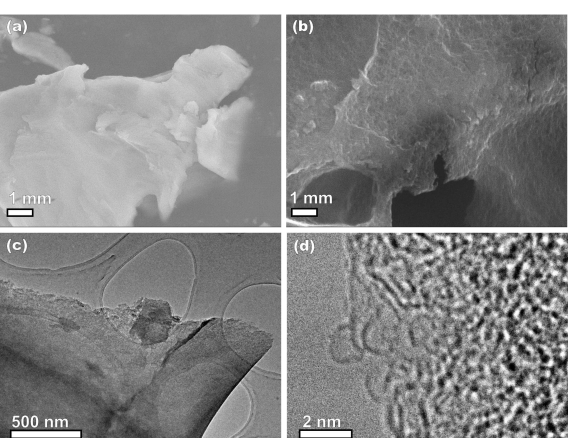


Figure 1. SEM images of the raw walnut shell (a) and the resulting shell-activated carbon (WAC) (b). Low (c) and high (d) magnification TEM images of WAC where fullerene-like configurations can be observed at the surface.

activation process (Figure 1b). Additionally, the transmission electron microscopy (TEM) study at low magnification (Figure 1c) reveals that the material comprises large, very thin carbon platelet-like particles. Upon closer inspection at higher magnification (HRTEM) in Figure 1d, it is evident that the material consists of highly disordered and entangled graphene layers serving as building units, with fullerene-like carbon layers apparent at the particle's edge.

The fresh synthesized MnO clusters (synthesis details in the experimental section) present high stability in aqueous solutions. These clusters can be identified as dark contrast spots with an average diameter of 2–4 nm along the TEM grid carbon support (Figure 2a) thanks to the electron energy loss spectroscopy (EELS) analysis performed on those areas, where the Mn and O peaks can be observed (Figure 2b). HRTEM images on the clusters confirm the MnO structure along the [011] and [100] zone axis, as indicated in Figures 2b and c.

Upon analysis, the crystal structure of MnO shows it resembles a cubic NaCl-type. This close-packed arrangement lacks atomic channels that can potentially serve as ionic channels and increase the total capacitance of the material, such as other different MnO_2 polymorphs. However, while MnO_2 is expected to have a higher theoretical specific capacitance due to the presence of those channels, it is fascinating to observe that MnO offers a superior value.^[19] This behavior can be ascribed to the close compact crystal structure of the MnO

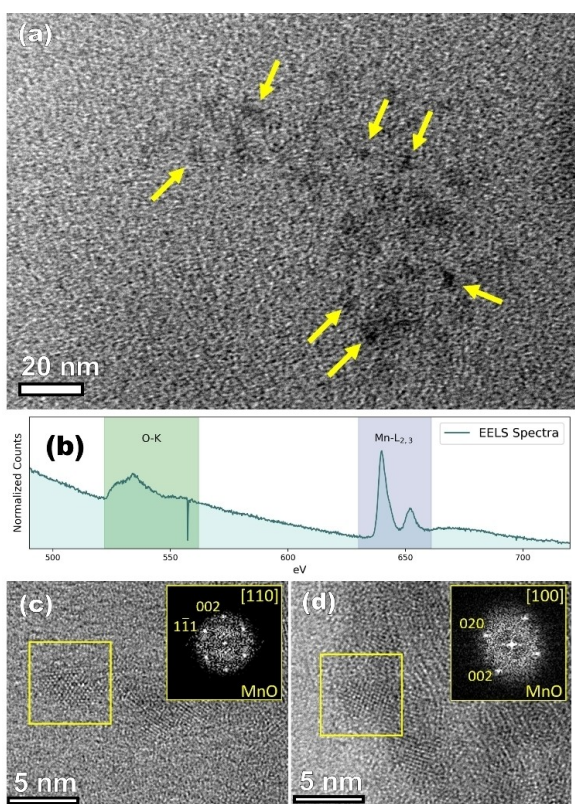


Figure 2. (a) Low magnification TEM micrograph of the colloidal MnO. (b) EELS analysis was performed over the area observed on panel (a), showing the Mn and O peaks. HRTEM images of the MnO clusters identified as MnO along the (c) [110] and (d) [100] zone axis. Inset of FFT performed on the areas highlighted on a yellow square.

that can offer a more robust and flexible ion exchange along the cluster surface. As such, it has gained recognition as one of the most promising electrode materials in developing supercapacitors.^[20]

The nanostructure of the MnO@WAC composite material, achieved by combining both components in a $1_{\text{MnO}}:99_{\text{WAC}}$ weight ratio, is analyzed in Figure 3. Initially, the low-magnification TEM (Figure 3a) does not reveal significant contrast variation to confirm the presence of MnO clusters within the particle. However, it's worth noting that the clusters are smaller than 4 nm in size and constitute only 1% of the weight. Nevertheless, the presence of the characteristic K_{α} peak at around 6 keV from manganese can be clearly detected by means of XEDS analyses conducted at low magnification areas of the AC particles such as shown on Figure 3b. To precisely determine the location, distribution, and appearance of the MnO clusters present within the carbon matrix, an advanced imaging technique known as scanning transmission electron microscopy in high-angle annular dark field mode (STEM-HAADF) was employed. The contrast in dark field mode can be considered proportional to the atomic number to the power of two. In this composite material, since Mn has the highest Z, we can identify the ultrasmall clusters of MnO as well as smaller clusters and isolated atoms as brighter spots well dispersed

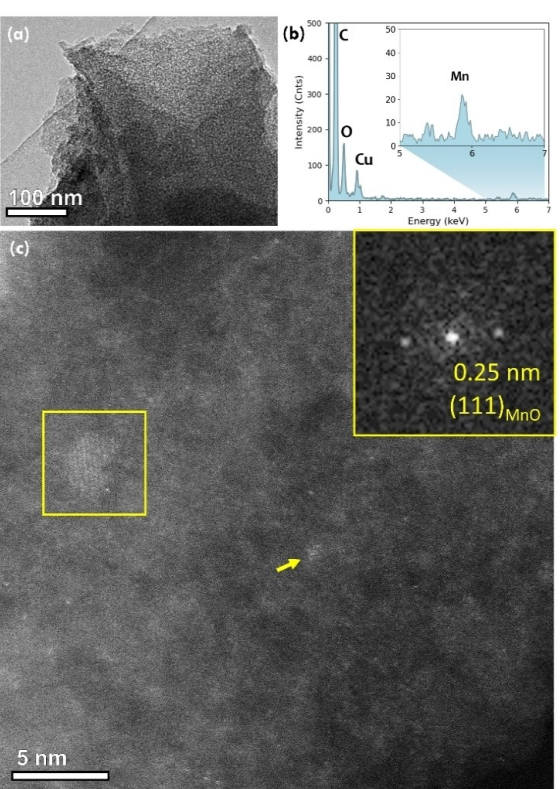


Figure 3. TEM image of MnO@WAC composite material at low magnification (a). XEDS spectrum of a whole carbon particle at low magnification (b), inset of a zoom area of the spectrum where the Mn peak it is clearly observed. High-resolution STEM-HAADF image of the composite material (c) where not only a MnO cluster can be observed, but also smaller clusters of few atoms (yellow arrow) and isolated ones along the entire AC matrix. Inset of the FFT performed over the particle highlighted by a yellow square, where the (111) plane distance of the MnO can be identified.

within the homogeneous darker contrast belonging to the carbon matrix (Figure 3c). Further high-resolution images were additionally performed along the entire sample to ensure the homogeneous distribution on the MnO clusters along the composite material (Figure S.2). The Fast Fourier Transform (FFT) performed on the particle highlighted in the yellow square in Figure 3c reveals a 0.25 nm interplanar distance of the MnO (111) lattice, confirming not only the presence of the clusters previous MnO clusters characterized on Figure 2, but also confirming that they do not experience any chemical transformation during their incorporation into the WAC matrix.

Preliminary cyclic voltammetry studies on the composite material with different nanoparticle loadings show a surface area reduction while increasing the nanoparticle content (Figure S.3a-c). To further evaluate the impact of cluster loading on the porous structure of the host material, N₂ adsorption-desorption isotherms were performed on both the WAC and MnO@WAC composite material at 77 K. The isotherm plots of both materials (Figure 4a) classify as type I according to the IUPAC classification, indicating that the porosity primarily consists of micropores (<2 nm), with slight deviations at high-pressure values suggesting the presence of particularly large pores.^[21] However, their impact on the total area is only around 5%, as reflected in the values for external surface area (S_{Ext}) shown in Table 2.

After incorporating 1% of MnO clusters, a reduction of 900 m² g⁻¹ in surface area was observed in Table 2 when compared to the textural parameters of both materials. Despite this decrease, the BET surface area values of these materials remain significantly higher than those reported for the same lignocellulosic precursor.^[22] The main difference between the

materials lies in the chemical activation process, which proves to be more effective in a solid mixture of carbon and KOH than in the impregnation of carbon in a KOH solution. The pore size distributions of WAC and MnO@WAC were derived from the NLDFT method^[23] and are illustrated in Figure 4b. The plots confirm that these materials display a well-defined pore structure composed of narrow (<0.7 nm) and broad (0.7-2 nm) micropores, with similar values as observed in Table 2. The primary difference found in the porous structures corresponds to the decrease in wide micropores with a size close to 2 nm, matching the lower size of the MnO clusters. Therefore, the reduction in surface area originates from the adsorption of MnO clusters within the micropores, aligning with their size.

Electrochemical Characterization

The high specific surface area and suitable porosity of both WAC and the MnO@WAC composite suggest their potential as electrode materials for electric double-layer capacitors (EDLCs). However, it's important to consider the influence of heteroatoms, such as oxygen or nitrogen, present on the surface of these materials.^[24] To mitigate any beneficial or harmful effects stemming from oxygen-containing functional groups, we opted for an aqueous neutral electrolyte (1 M KCl) in our electrochemical evaluation. This choice is supported by previous studies indicating that oxygen-containing functional groups have a limited impact on the energy storage of supercapacitors with neutral electrolytes, whereas they play a significant role in systems utilizing strongly acidic or alkaline electrolytes.^[25] Prior to characterization, different electrolytes were tested (Fig-

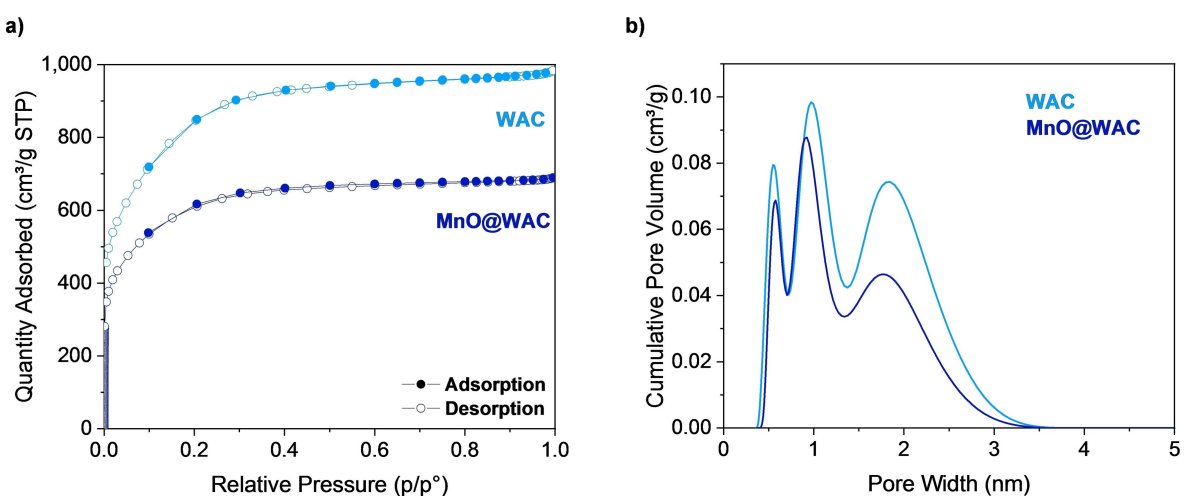


Figure 4. N₂ isotherm plots of WAC and MnO@WAC (a). Pore size distributions, focusing on the region with pore widths ≤ 5 nm (b).

Table 2. Total, external, and micropore BET surface area and pore width of WAC and MnO@WAC.

	S _{Total} (m ² ·g ⁻¹)	S _{Ext.} (m ² ·g ⁻¹)	S _{Micr.} (m ² ·g ⁻¹)	Pore Width _{2D-NLDFT} (nm)
WAC	2927	140	2786	0.55, 0.97 & 1.82
MnO@WAC	2070	84	1985	0.57, 0.92 & 1.76

ure S3d), an aqueous neutral KCl 1 M electrolyte was selected to evaluate the electrochemical performance of our materials.

Figure 5a shows the cyclic voltammetry (CV) profiles recorded at 5 mVs⁻¹ scan rate for the bare WAC carbon and the composite MnO@WAC in KCl. The CV curves for both materials, show rectangular and symmetric profiles typical of pure capacitive behaviour. A closer inspection in the shapes of the CVs, denotes that the CV of WAC is slightly distorted, that can be ascribed to the inherent resistivity of the electrode,^[26] in comparison with the curve of MnO@WAC, suggesting that the incorporation of just 1% of MnO in the carbon material provokes an improvement on the electrode conductivity. Moreover, with the escalation of the sweep rate (Figure S.4a), the shape and the area under the curve of the cyclic voltammograms (CVs) of MnO@WAC are nearly maintained. In contrast, for WAC, there is a more conspicuous loss of shape, and the area under the CV curve decreases more rapidly, indicating a poorer capacitance retention in the absence of MnO clusters within the carbon material.

The electrochemical performance of WAC and the MnO@WAC nanocomposite was further evaluated through galvanostatic charge-discharge measurements (GCPL) conducted in the current density range from 0.1 to 10 A g⁻¹ (Figure S.4c). All

curves exhibit a symmetrical feature between the charging and discharging branches, suggesting an ideal capacitive nature of fast charge/discharge processes,^[27] consistent with the CV results.

At 0.1 A g⁻¹ (Figure 5b), capacitance values calculated from GCPL indicate a higher gravimetric capacitance value for the carbon material compared to the composite: 195 Fg⁻¹ for WAC and 157 Fg⁻¹ for MnO@WAC, respectively (refer to Table S.1 and S.2). This disparity suggests that the carbon material possesses a 24% higher capacitance value than the nano-composite MnO@WAC, likely due to the deposition of clusters within the composite, resulting in a 29% decrease in surface area (see Table 2) and thus reduced accessibility of the surface to electrolyte ions. However, at current densities exceeding 1.5 A g⁻¹ up to 10 A g⁻¹, both the gravimetric and volumetric capacitances of MnO@WAC remain almost constant, whereas WAC experiences a significant reduction in capacitance within the same range (see Figure 5c and S.4b). Since both materials exhibit a similar pore size distribution well-suited to accommodate KCl ions, it appears that the pseudocapacitive contribution of such clusters helps offset the loss of pure capacitance, with a more pronounced impact at high current densities. This capacitance fading may also be related to the higher IR drop

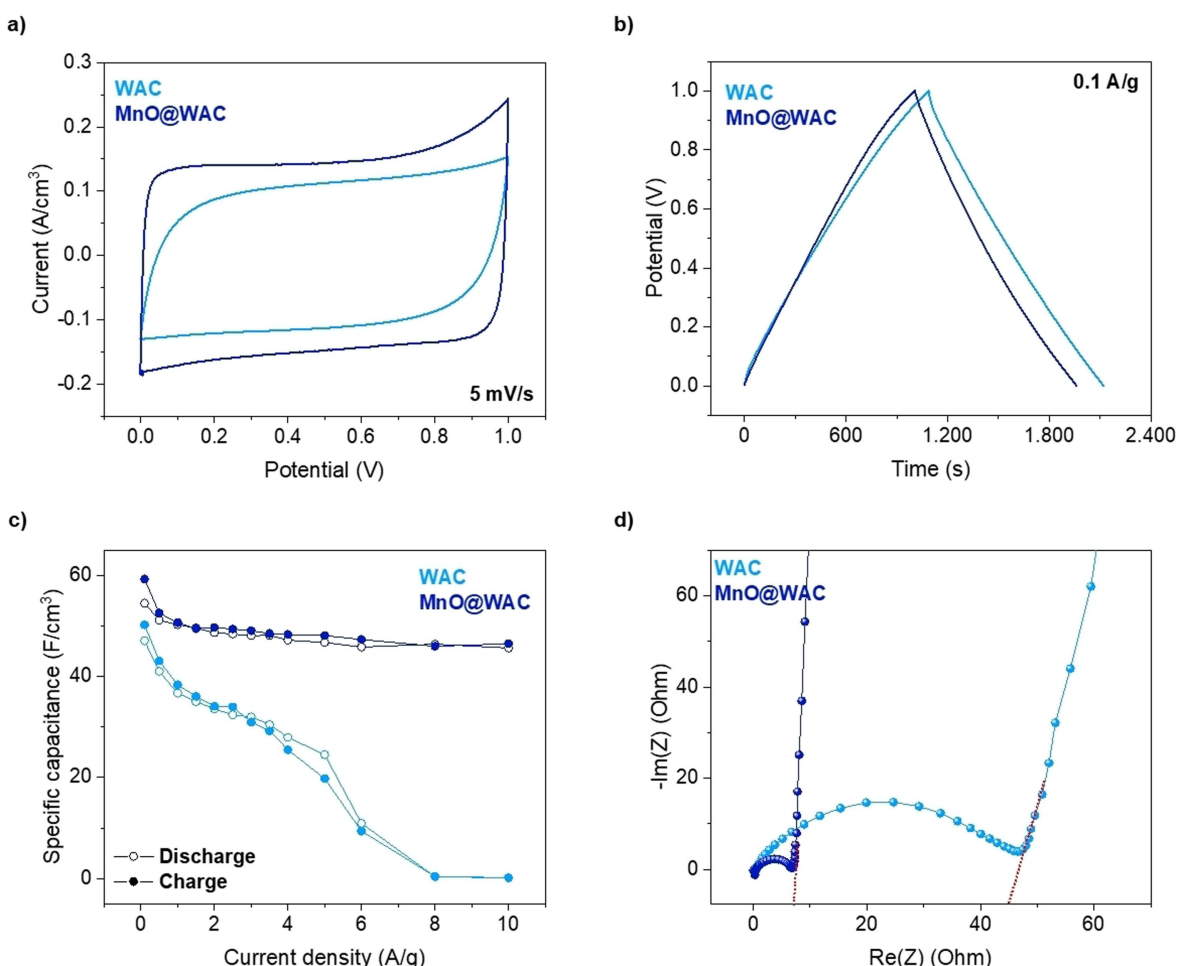


Figure 5. (a) Cyclic voltammograms at 5 mV/s, (b) galvanostatic charge-discharge cycles, (c) volumetric capacitances retention as a function of the current density and (d) Nyquist plots of WAC and MnO@WAC on a symmetric two-electrode cell.

measured in WAC compared to MnO@WAC, being 0.004 and 0.002 V at 0.1 A g^{-1} and 0.27 and 0.06 V at 2 A g^{-1} , respectively (Figure S.4c). This behavior underscores the benefit of incorporating such a small amount of MnO clusters within the carbon matrix.

In addition, since the density of the composite MnO@WAC is higher than the one for WAC, 0.35 and 0.25 g cm^{-3} respectively, the volumetric capacitance of the nanocomposite is higher than the carbon material in the whole range of current density (Figure 5c). More benefits of the incorporation of 1% of MnO can be evidenced by electrochemical impedance spectroscopy (EIS) which provides the resistance and capacitance of a supercapacitor from the frequency response.^[28]

The Nyquist plots obtained from potentiostatic electrochemical impedance spectroscopy (PEIS) measurements are depicted in Figure 5d, showcasing the typical curves associated with porous carbon electrodes. Since the construction of the two supercapacitors only differs in the nature of the electrode materials, the electrical series resistance (ESR) calculated from the intersection on the real axis of the Nyquist plot in the high-frequency region primarily reflects the bulk electrode conductivity. It is evident that the MnO@WAC composite exhibits a much smaller diameter of the Nyquist semicircle, indicating a significantly more efficient charge transfer process at the electrode interface. The equivalent distributed resistance (EDR), determined by linear projection from the vertical portion of the Nyquist plot to the real axis, represents ion diffusion through carbon pores. MnO@WAC demonstrates an EDR value of 7 Ohms, much smaller than the 45 Ohms determined for WAC. Therefore, one can conclude that the presence of MnO clusters offers a less resistive surface for ion diffusion, consistent with the GCPL results.

From the PEIS it is possible to derive the real and imaginary parts of capacitance (details for calculations on SI).^[29] The plot of the real capacitance $C'(\omega)$ (see Figure 6a) shows in the case of MnO@WAC a clear transition between purely resistive to purely capacitive behavior, whereas in the case of WAC the transition is not completed even at the lowest frequencies. On the other hand, the plot of the imaginary capacitance $C''(\omega)$ (see Fig-

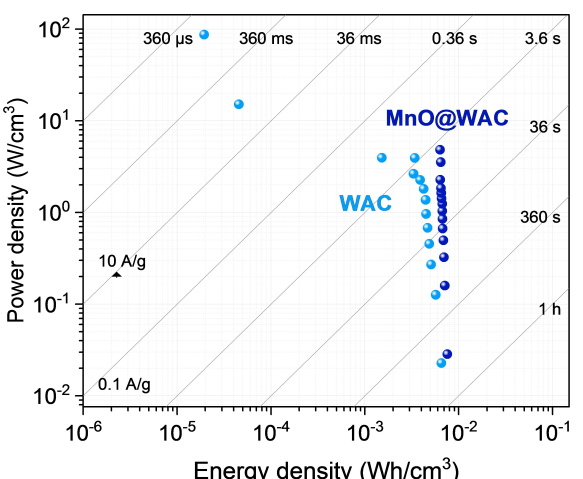


Figure 7. Volumetric Ragone plots obtained with symmetric WAC and MnO@WAC capacitors working at 1 V applying current densities from 0.1 to 10 A g^{-1} in KCl 1 M.

ure 6b), exhibits a curve shape where the maximum can be roughly described as the point where the circuit goes from purely resistive to purely capacitive. The inverse of the frequency at this point yields a time constant that is a quantitative measure of how fast the device can be charged and discharged reversibly, being seven times faster in MnO@WAC (10 and 68 s respectively).

The discrepancies in resistance observed among the supercapacitors are poised to impact their power density due to the inverse relationship between power and resistance. Utilization of Ragone plots, which delineate the connection between power density and energy density, can be further employed to highlight the influence of the incorporation of 1% of MnO clusters on the electrochemical performance.^[30] Figure 7 depicts the volumetric Ragone plot obtained with symmetric WAC and MnO@WAC supercapacitors at a practical voltage of 1 V in KCl 1 M. We observe that MnO@WAC yields higher energy densities than WAC with stable values varying between 7.6 – 6.3 mWh cm^{-3} (22 – 18 Wh g^{-1} in gravimetric units see Table S.2) in the

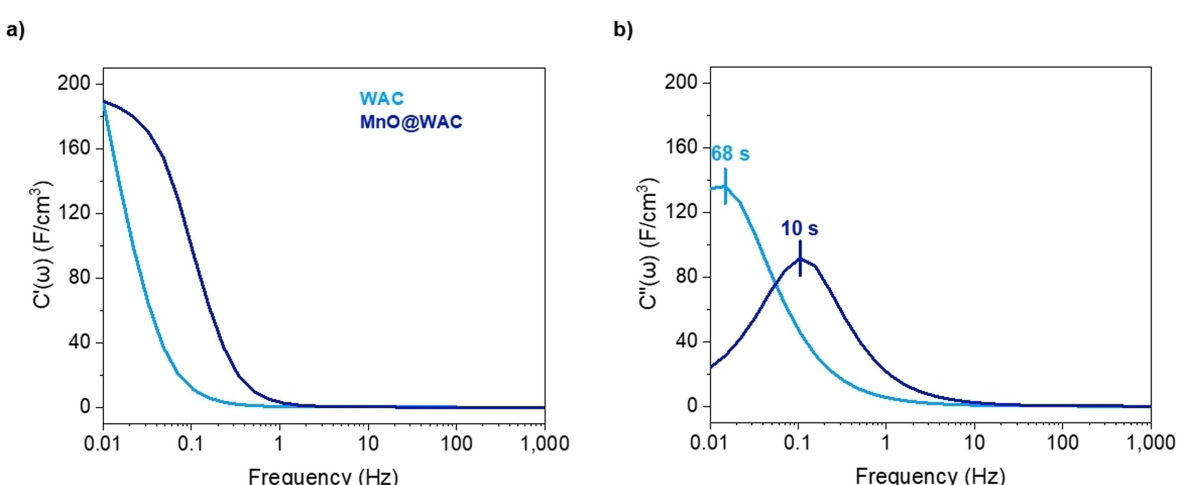


Figure 6. Evolution of the (a) real part and (b) imaginary capacitance vs. frequency for WAC and MnO@WAC supercapacitors.

whole range of power density, however in the case of WAC the energy density suffers a dramatic drop at high-power densities (see Table S.1). These results probe that a very small amount of MnO clusters can enhance the electrochemical performance of a carbon material making it more competitive for commercial applications.

Conclusions

A Novel MnO@WAC composite material has been successfully synthesized by the combination of activated nanoporous carbon with an enormous specific surface area from Galician walnut shells (WAC) obtained by dry chemical activation with ultrasmall MnO clusters synthesized by a direct method using polyacrylic acid as both surfactant and reduction agent. The combination of these materials in precise proportions results in a composite material that boasts superior electrochemical performance. This is attributed to the pseudocapacitive attributes of MnO clusters, which complement the capacitive mechanism of WAC. Additionally, the electrical conductivity of the composite material is heightened, as demonstrated by a noteworthy reduction in ESR value recorded through impedance measurements. Despite a decrease in surface area, the MnO@WAC composite exhibits enhanced capacitive behavior, outperforming pure WAC on capacitance retention at higher current densities, highlighting its potential as a high-performance electrode for supercapacitors. This study showcases the feasibility of utilizing renewable biomass for nanomaterial composite design for sustainable energy storage applications.

Experimental Section

Materials

Walnut shells were obtained from the rural area of Galicia, Spain. KOH and HCl for AC synthesis, as well as polyacrylic acid (PAA) and KMnO₄ salt for nanoparticle synthesis and KCl salt for the liquid electrolyte, supplied by Sigma Aldrich. Milli-Q grade water was employed for both nanoparticle synthesis and electrolyte solution.

Synthesis

To prepare the activated carbon (AC), the walnut shells underwent a crushing process in a metal mortar to reduce their size to millimeters. Subsequently, 5 g of these crushed particles were placed into a quartz crucible and subjected to heating at 400 °C for 10 minutes in a tubular furnace under an argon (Ar) atmosphere to eliminate low boiling and melting point organic compounds. Once carbonization was complete, the heating was turned off, and the system was allowed to cool to room temperature. For the activation step, the carbon powder was mixed thoroughly with KOH in a 1:4 ratio. This mixture was then placed in an alumina crucible inside a tubular furnace under an Ar atmosphere and heated at 700 °C for 60 minutes. After activation, the heating was stopped, and the system was cooled to 25 °C. The activated carbon, labeled as WAC, was subsequently neutralized using concentrated HCl solution and washed with distilled water until all chemical impurities were

completely removed. The resulting product, designated as WAC, was then dried in an oven at 110 °C for 24 hours.

Manganese oxide (MnO) clusters were synthesized through a novel method using polyacrylic acid (PAA) as both a surfactant and a reducing agent for manganese derived from KMnO₄. To a solution containing 20 mL of 0.02 M KMnO₄, 1.2 mmol of PAA was added. Within minutes, the solution transitioned from purple to light brown, indicating the reduction of manganese oxidation state and the formation of a colloidal solution of MnO clusters. The colloid was then dialyzed for 5 days with continuous stirring, with daily water renewal to eliminate excess PAA. Subsequently, the final colloid dispersion underwent washing through centrifugation (4,000 rpm, 60 min) and was then dried overnight at 80 °C, yielding a brown powder as the MnO clusters product.

For the preparation of the MnO@WAC composite material, a dispersion containing MnO clusters in 5 mL of water was combined with an aqueous suspension of WAC (5 mL) in a weight ratio of 1:100. After thorough mixing, the mixture was sonicated for 5 minutes, resulting in a color change from brown to transparent, indicating the incorporation of MnO clusters within the activated carbon. The MnO@WAC composite was isolated via centrifugation (6,000 rpm, 15 min) and subsequently dried overnight at 80 °C.

Characterization

Infrared spectra were collected using a PerkinElmer 100 FT-IR spectrometer across the range of 4,000–650 cm⁻¹. Textural characterization was conducted through N₂ adsorption studies at 77 K using a surface area and porosity analyzer ASAP2020 (Micromeritics). The specific surface area (S_{BET}) was determined using BET theory, and pore size distribution (PSDs) was calculated utilizing the SAEIUS software for 2D nonlocal density functional theory (2D-NLDFT), considering energetically heterogeneous pore walls in the standard carbon slit-shaped pore geometry.

Scanning Electron Microscopy (SEM) images were captured using a JSM 6335 F electron microscope operating at 15 kV and a working distance of 15 mm. Low-magnification TEM studies and EDS analysis were performed using a JEOL 3000 F microscope with an acceleration voltage of 300 kV. High-resolution high-angle annular dark field scanning transmission electron microscopy (HAADF-STEM) images were acquired using an aberration-corrected Thermo Fisher Titan microscope operated at 300 kV.

Electrochemical characterization involved the use of a two-electrode Swagelok-type cell with disk-shaped electrodes. The electrodes were prepared by mixing 95 % of the carbon/composite material with 5 % of a polytetrafluoroethylene solution (PTFE 60%, Sigma-Aldrich) as a polymer binder. The resulting mixture was stirred gently with ethanol until achieving a smooth and viscous texture. A glass test tube was used to uniformly laminate the slurry to ensure a final thickness of 250–200 µm. The film was then dried and kept under vacuum at 120 °C for 12 hours before each measurement. The electrodes, 10 mm in diameter and of comparable mass, were assembled in a symmetrical Swagelok-type cell, wetted with the electrolyte, separated with a glass fiber membrane (Whatman glass microfiber filters, grade GF/B, 12.7 mm in diameter), and placed in direct contact with the Ti current collector.

Electrochemical experiments were conducted in a 1 M aqueous KCl solution within a voltage range of 0 to 1 V versus RHE. Cyclic voltammetry (CV) was performed with a scan rate of 5 mV/s, while galvanostatic measurements were taken at current densities ranging from 0.1 to 10 A/g. The experiments were conducted under normal conditions using a multichannel potentiostat/galvanostat (Biologic VMP3). Electrochemical Impedance Spectroscopy (EIS) was

performed by applying a low sinusoidal voltage of 10 mV to the working electrode. Frequencies ranged from 1 MHz to 10 mHz, with the multichannel potentiostat/galvanostat used at the open circuit potential (OCP). The specific capacitance (C_{grav}) of the working electrode was calculated from the galvanostatic charge-discharge plot using the following equation:

$$C_{grav} = \frac{2It}{m_e \Delta E_{cell}}$$

where I is the current (A), m_e refers to the mass (g) of active material in a single electrode, t is the charge or discharge time (s), and ΔE_{cell} is the potential (V vs. SHE) between the WE and RE. The volumetric capacitance was obtained by multiplying the gravimetric capacitance by the density ρ (g cm⁻³) of the electrode film, which was calculated by dividing the electrode mass by its volume.

$$C_{vol} = C_{grav} \cdot \rho$$

Acknowledgements

Grants PID2020-112848RB-C21 funded by MCIN/AEI/10.13039/501100011033 and by the European Union PRTR funding through projects are acknowledged. Access to the ICTS-CNME for TEM is also acknowledged.

Conflict of Interests

The authors declare no conflict of interest.

Data Availability Statement

The data that support the findings of this study are available on request from the corresponding author. The data are not publicly available due to privacy or ethical restrictions.

Keywords: Activated Carbons • Supercapacitors • Composite materials • Porous Materials • Energy Storage

- [1] M. M. Rahman, A. O. Oni, E. Gemedu, A. Kumar, *Energy Convers. Manage.* **2020**, 223, 113295.
- [2] P. Simon, Y. Gogotsi, *Nat. Mater.* **2008**, 7, 845–854.
- [3] J. M. Lim, Y. S. Jang, H. V. T. Nguyen, J. S. Kim, Y. Yoon, B. J. Park, S. G. Doo, *Nanoscale Adv.* **2023**, 5(3), 615–626.
- [4] A. Burke, *Electrochim. Acta* **2007**, 53, 1083–1091.

- [5] a) A. Ip, J. Barford, G. McKay, *Biores. Tech.* **2008**, 99(18), 8909–8916; b) C. Long, D. Qi, T. Wei, J. Yan, L. Jiang, Z. Fan, *Adv. Funct. Mater.* **2014**, 24, 3953–3961; c) H. Wang, Z. Xu, A. Kohandehghan, Z. Li, K. Cui, X. Tan, T. J. Stephenson, C. K. King, C. M. B. Holt, B. C. Olsen, J. K. Tak, D. Harfield, A. O. Anyia, D. Mitlin, W. E. T. Ai, *ACS Nano* **2013**, 7(6), 5131–41; d) E. Redondo, J. Carretero-González, E. Goikolea, J. Ségalini, R. Mysyk, *Electrochim. Acta* **2015**, 160, 178–184; e) A. M. Navarro-Suárez, J. Carretero-González, V. Roddatis, E. Goikolea, J. Ségalini, E. Redondo, T. Rojo, R. Mysyk, *RSC Advances* **2014**, 4(89), 48336–48343.
- [6] L. Wei, M. Sevilla, A. B. Fuertes, R. Mokaya, G. H. Yushin, *Adv. Energy Mater.* **2011**, 1, 356–361.
- [7] Y. Gogotsi, P. Simon, *Science* **2011**, 334, 917.
- [8] V. Molahalli, K. Chaithrashree, M. K. Singh, M. Agrawal, S. G. Krishnan, G. Hegde, *Journal of Energy Storage* **2023**, 70, 108062.
- [9] P. Simon, Y. Gogotsi, *Nat. Mater.* **2008**, 7, 845–854.
- [10] J. Wang, S. Dong, B. Ding, Y. Wang, X. Hao, H. Dou, Y. Xia, X. Zhang, *Nat. Sci. Rev.* **2017**, 4(1), 71–90.
- [11] S. Fleischmann, J. B. Mitchell, R. Wang, C. Zhan, D. E. Jiang, V. Presser, V. Augustyn, *Chem. Rev.* **2020**, 120(14), 6738–6782.
- [12] W. Sugimoto, K. Yokoshima, Y. Murakami, Y. Takasu, *Electrochim. Acta* **2006**, 52(4), 1742–1748.
- [13] B. E. Conway, (1999). *Electrochemical Supercapacitors*. Kluwer Academic.
- [14] Y. Pei, D. P. Wilkinson, E. Gyenge, *Small* **2023**, 19, 2204585.
- [15] a) T. Bordjiba, D. Bélanger, *J. Electrochem. Soc.* **2009**, 156(5), A378–A384; b) L. Chen, X. Guo, W. Lu, M. Chen, Q. Li, H. Xue, H. Pang, *Coord. Chem. Rev.* **2018**, 368, 13–34; c) D. Qu, X. Feng, X. Wei, L. Guo, H. Cai, H. Tang, Z. Xie, *Appl. Surf. Sci.* **2017**, 413, 344–350.
- [16] J. Liu, J. Bao, X. Zhang, Y. Gao, Y. Zhang, L. Liu, Z. Cao, *RSC advances* **2022**, 12, 35556–35578.
- [17] P. González-García, T. A. Centeno, E. Urones-Garrote, D. Ávila-Brande, L. C. Otero-Díaz, *Appl. Surf. Sci.* **2013**, 265, 731–737.
- [18] T. A. Centeno, F. Stoeckli, *Electrochim. Acta* **2006**, 52(2), 560–566.
- [19] M. -Yang, Y. Zhong, X. Zhou, J. Ren, L. Su, J. Wei, Z. Zhou, *J. Mater. Chem. A* **2014**, 2(31), 12519–12525.
- [20] W. Wei, X. Cui, C. Weixing, D. G. Ivey, *Chem. Soc. Rev.* **2011**, 40(3), 1697–1721.
- [21] M. A. Al-Ghouti, D. A. Da'ana, *Journal of hazardous materials* **2020**, 393, 122383.
- [22] S. J. Gregg, K. S. W. Sing, (1982). Adsorption, surface area and porosity. Academic Press, London.
- [23] J. Jagiello, C. Ania, J. B. Parra, C. Cook, *Carbon* **2015**, 91, 330–337.
- [24] N. Yuan, G. Maoqiang, Z. Yuting, Y. Jie, et al. *Journal of Energy Storage* **2023**, 73, C 109064.
- [25] C. Qiu, L. Jiang, Y. Gao, L. Sheng, *Materials & Design* **2023**, 230, 111952.
- [26] K. Wang, Y. Wang, Y. Wang, E. Hosono, H. Zhou, *J. Phys. Chem. C* **2008**, 113, 1093–1097.
- [27] J. Fei, et al. *Adv. Mater.* **2008**, 20, 452–456.
- [28] Poonam, M. Vyas, D. K. Jangid, R. Rohan, K. Pareek, *Energy Storage* **2022**, 4, 5, e355.
- [29] P. L. Taberna, P. Simon, J. F. Fauvarque, *J. Electrochem. Soc.* **2003**, 150 A292.
- [30] I. Beyers, A. Bensmann, R. Hanke-Rauschenbach, *Journal of Energy Storage* **2023**, 73, 109097.

Manuscript received: February 13, 2024

Revised manuscript received: March 11, 2024

Accepted manuscript online: March 17, 2024

Version of record online: April 8, 2024